Additive Manufacturing 46 (2021) 102085

Contents lists available at ScienceDirect

Additive Manufacturing

journal homepage: www.elsevier.com/locate/addma

Ultra-short pulsed laser powder bed fusion of Al-Si alloys: Impact of pulse duration and energy in comparison to continuous wave excitation

Tobias Ullsperger [a,*], Dongmei Liu [c], Burak Yürekli [a], Gabor Matthäus [a], Lisa Schade [a], Brian Seyfarth [a,b], Hagen Kohl [a], Roland Ramm [b], Markus Rettenmayr [c], Stefan Nolte [a,b]

[a] Institute of Applied Physics, Abbe-Center of Photonics, Friedrich Schiller University Jena, Albert-Einstein Strasse 15, 07745 Jena, Germany
[b] Fraunhofer Institute for Applied Optics and Precision Engineering, IOF, Center of Excellence in Photonics, Albert-Einstein Strasse 7, 07745 Jena, Germany
[c] Otto Schott Institute of Material Research, Friedrich Schiller University Jena, Löbdergraben 32, 07743 Jena, Germany

ARTICLE INFO

Keywords:
Laser powder bed fusion
Additive manufacturing
Ultra-short laser pulses
Hypereutectic Al-Si alloys
Rapid solidification

ABSTRACT

Laser assisted powder bed fusion of Al-40 wt%Si using ultra-short laser pulses is presented. The effects of the pulse duration as well as the pulse energy on the melt pool size, solidification morphology and material properties have been investigated. The experiments have been carried out with a mode-locked fiber laser system delivering pulses from 500 fs up to 800 ps at a wavelength of 1030 nm. Comparative investigations have been performed using a continuous wave Yb-fiber laser operating at 1070 nm. The results show that the melt pool width is reduced at shorter pulse durations and higher repetition rates while maintaining the same average power. Additionally, keyhole melting is achieved in pulsed operation after exceeding the threshold fluence for single pulse ablation. In comparison to continuous wave radiation, powder bed fusion using ultra-short laser pulses leads to a more uniform melt pool shape with refined primary Si and eutectic structure that is accompanied with an improvement of the mechanical properties.

1. Introduction

The fast development in additive manufacturing of metals revolutionizes the way of modern industrial production. One of the most promising techniques for the fabrication of customized near net shape metal components is laser assisted powder bed fusion (L-PBF) [1,2]. In conventional devices, powder particles are selectively fused layer-wise using a continuous wave (cw) laser [3,4]. However, in recent years the application of intense ultra-short laser pulses (USP) revealed an enormous potential to extend the material variety in additive manufacturing [5–10]. Such pulses in the range of femto- to picoseconds are commonly used for low damage ablation in micro-machining applications, leading to a significantly smaller heat-affected zone [11,12]. However, a small amount of energy still remains in the material [13], and if the time between two consecutive pulses is far shorter than the characteristic thermal diffusion time, heat is accumulated and the temperature is continuously rising [14]. This effect is especially used for local welding of transparent materials [15–17]. Previous research has shown that the heat accumulation combined with high peak powers of USPs is beneficial for melting metal powders with a high melting point or a high reflectivity, such as tungsten and pure copper [5–9]. Furthermore, the application of ultra-short pulsed L-PBF to binary aluminum silicon (Al-Si) alloys with silicon (Si) concentrations of up to 70 wt% has led to significant refinement of the primary Si-phase [10,18], which is supposed to contribute to improved mechanical properties.

The object of the present investigation is L-PBF of binary Al- 40 wt% Si (in the following Al-40Si) alloy. Al-40Si is a promising material for weight-reduced metal mirrors used for space applications [19]. It is easier to process than other competing materials such as beryllium or titanium alloys. To achieve the roughness required for the undisturbed and aberration-free reflection of visible and ultraviolet light, the optical relevant surface of the metal mirror is coated with an amorphous nickel phosphor (NiP) layer. The coefficient of thermal expansion (CTE) of Al-40Si, approximately $13 \cdot 10^{-6}$ K^{-1} (–50 to 100 °C) [20], is comparable with that of NiP, which prevents bi-metallic bending and contributes to a stable configuration in the presence of the pronounced temperature fluctuations in space. Additionally, the high elastic modulus of Al-40Si of 93–102 GPa [20,21], the high ultimate tensile strength of 220–300 MPa [20–22] in combination with the low density of 2.54 g/cm^3 [21] makes Al-40Si particularly stiff and mechanically robust. According to

* Corresponding author.
E-mail address: tobias.ullsperger@uni-jena.de (T. Ullsperger).

https://doi.org/10.1016/j.addma.2021.102085
Received 16 October 2020; Received in revised form 12 March 2021; Accepted 27 May 2021
Available online 29 May 2021

the phase diagram of Al-Si (see Fig. 1(a)), the solidification interval, i.e. the difference between the liquidus and solidus temperature is $\Delta T \approx 340$ K [23]. The low cooling rate during conventional casting leads to coarse primary Si plates in the as-cast microstructure (see Fig. 1(b)), which has an unfavorable effect on the mechanical and thermal properties. For refining the primary Si crystals in Al-40Si, rapid solidification processes, such as melt spinning, spray forming [24,25] (see Fig. 1(c)), L-PBF [19,20,22] (see Fig. 1(d)) and micro cladding using conventional cw laser sources [26–28] have been already performed. In contrast to spray forming (Fig. 1(c)), L-PBF (Fig. (d)) leads to much finer primary Si crystals and a more homogenous Si distribution. In comparison to conventional cw laser, ultra-short laser pulses lead to confined melt pool widths of less than 100 μm, and due to faster heat extraction from the melt pool to a finer microstructure and better mechanical properties [10,18]. However, up to now a fundamental comparison of the L-PBF process between cw and ultra-short pulses at the same applied average power and energy density is still lacking. In the present work, the influence of the pulse duration and pulse energy in comparison to cw laser irradiation on the size and shape of the melt pool during L-PBF of Al-40Si is investigated. Solidification microstructure and hardness of the samples are analyzed and correlated with the L-PBF process parameters.

2. Materials and methods

2.1. Powder

Al-Si powder produced by gas-atomization of an Al-40Si melt provided by the company TLS- Technik was used. The powder particles are of approximately spherical shape as shown in Fig. 2(a). Concluding from the size of the particles, the estimated cooling rate during gas-atomization is $> 10^2$ K/s [29]. Upon closer observation of the cross section of a particle using Back-scattered electron (BSE) contrast, elongated primary Si plates (white phase) with lengths from 2 to 15 μm are found, forming a Si shell at the surface of the particle (see Fig. 2(b)). This leads to the depletion of Si at the solidification front growing towards the center of the particle. Subsequently, α-Al dendrites (grey phase) precipitate from the melt, and finally interdendritic eutectic forms. The particle distribution was determined by optical granulometry of single powder layers, considering a total number of analyzed particles of ≈ 100,000 with the help of ImageJ software [30,31]. The obtained monomodal distribution ranging from 16 μm (D_{10}) to 56 μm (D_{90}) with a mean diameter of 35 μm (D_{50}) is shown in Fig. 2(c).

2.2. Laser powder bed fusion system

The L-PBF process was carried out using two different setups. The cw experiments were performed using a commercial L-PBF machine by Concept Laser GmbH (M2) equipped with a 400 W Yb-fiber laser (IPG Photonics) operating at 1070 nm. The laser beam was focused with a 400 mm F-Theta lens to a minimum spot diameter of 50 μm. The USP experiments were conducted using a custom-made setup based on the same working principle as the M2, which, however, allows a flexible change of the laser source, scanner and focusing lens. For the present experiments a galvano-scanner (HurryScan14 by Scanlab) equipped with an F-theta lens of 160 mm focal length is used. In both configurations the powder is spread with a re-coater (rubber blade) from the reservoir to the build stage. During the L-PBF process, the chambers are filled with nitrogen to avoid oxidation, maintaining an oxygen concentration < 0.3 vol%.

The femtosecond laser source used in the experiments was a fiber laser (by Active Fiber Systems GmbH) operating at 1030 nm. A passively mode-locked seed fiber laser generates pulses with a duration of 500 fs at a repetition rate of 20 MHz. An acousto-optical modulator (AOM) picks every n-th (n ϵ N) pulse and thus controls the desired repetition rate for the experiment. The pulses are propagating through a grating stretcher, that generates a down-chirp resulting in an increase of the pulse duration to 800 ps before passing the amplification stage to avoid damage of the optical components (chirped pulse amplification, CPA). After amplification, the pulses can be re-compressed using an adjustable grating compressor, yielding pulse durations from 500 fs to 20 ps. Alternatively, the compressor can be bypassed to obtain pulses with 800 ps duration. The maximum pulse energy obtained is 100 μJ at 500 kHz. A second AOM is used as a shutter and to adjust the pulse energy.

2.3. Absorption of short and ultra-short laser pulses

During the interaction of ultra-short laser pulses with metals such as Al, the quasi-free electrons with a density of $1.8 \cdot 10^{23}$ cm^{-3} in the conduction band, first absorb the photons via inverse bremsstrahlung [32]. In contrast to that, Si is an indirect semiconductor with a bandgap energy of 1.12 eV [33] at 300 K, corresponding to a wavelength of 1100 nm. The intrinsic carrier density of Si increases with rising temperature (10^{10} to 10^{19} cm^{-3}) [33,34], which however is still several orders of magnitude lower than for metals. Due to the indirect linear photon absorption with the help of an additional phonon, the absorption coefficient of Si at a wavelength of 1030 nm is around 30 cm^{-1} [35]. The intensities of the focused ultra-short laser pulses in the presented work are in the order of 10^8 to 10^{11} W/cm^2. This leads to an excitation of additional electrons to the conduction band by multi-photon absorption and subsequent avalanche ionization [36]. After the excitation, the electrons in Al and Si transfer their energy via phonon interaction to the lattice and the crystal heats up [11,12]. The characteristic electron-phonon coupling time is in the range of a few picoseconds [37,38]. In this regard, three different pulse regimes of durations ranging from 500 fs to 800 ps together with cw radiation are used in the present

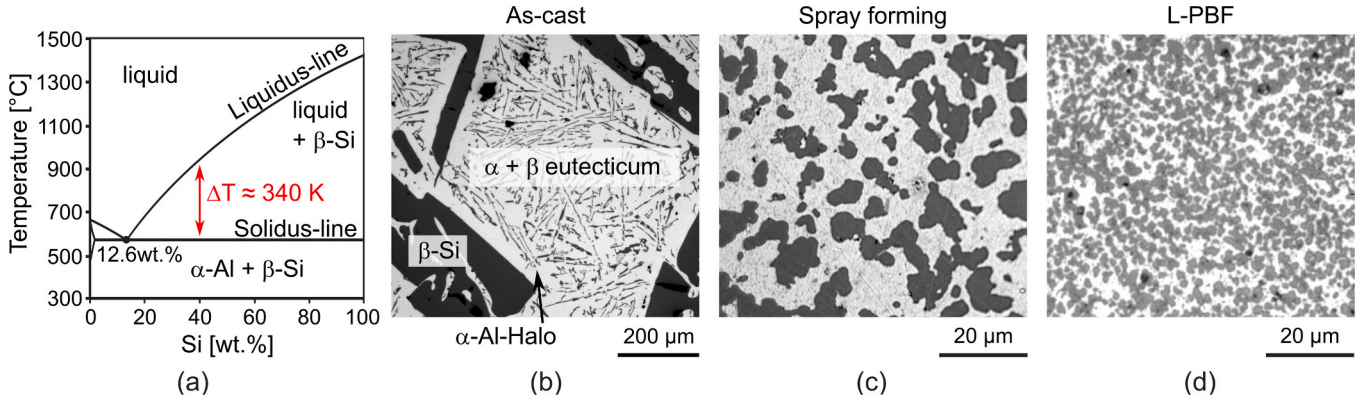

Fig. 1. Al-Si phase diagram [22] (a). Microstructure of as-cast Al-40Si (b), Al-42Si (CE13) produced by spray forming (Osprey Sandvik) (c) and Al-40Si after L-PBF [20] (d).

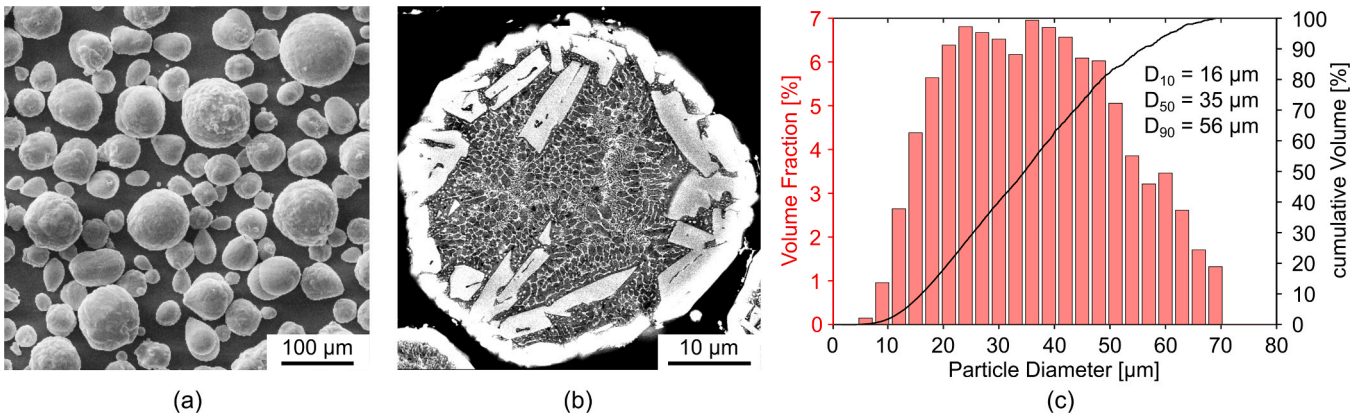

Fig. 2. (a) SEM image of Al-40Si powder; (b) BSE image of the cross section of a powder particle; (c) particle size distribution obtained using optical granulometry.

work for addressing the different kinds of excitation. Pulses with a duration 500 fs represent an ultra-short pulse duration, where most of the pulse energy is absorbed by the electrons, before the relaxation with the lattice system occurs [11]. Here, two decoupled temperatures can be addressed. The second pulse duration of 20 ps was used as a temporal transition zone in a later stage of the electron-lattice relaxation, whereas with the third pulse duration of 800 ps ("short pulses"), electrons and lattice can be described by a common temperature and a significant amount of energy dissipates through thermal diffusion already during the pulse duration.

2.4. Laser parameters

The objective of this study is the investigation of the limits using ultra-short laser pulses, the melt pool shape, as well as the solidification morphology of Al-40Si depending on the pulse duration and pulse energy in comparison to cw during L-PBF. Some crucial laser parameters are kept constant to ensure better comparability (see Table 1).

The spot diameter d_S ($1/e^2$) on the surface of the powder bed was set to 50 µm and the applied average power P_{av} was 25 W for all experiments. The resulting maximum average laser intensity I_0 in all cases is given by Eq. 1:

$$I_0 = \frac{8\,P_{av}}{\pi\,d_S^2} = 2.55 \times 10^6 \frac{\mathrm{W}}{\mathrm{cm}^2} \tag{1}$$

In contrast to cw radiation, the average power delivered by the laser pulses is modulated in terms of their repetition rate f_{rep} and pulse energy E_P given by Eq. 2:

$$P_{av} = E_P \times f_{rep} \tag{2}$$

Together with the length of the pulse duration, short and ultra-short laser pulses allow an extreme temporal power modulation. The experiments were performed using three different pulse durations that are mentioned in the previous section. The ultra-short pulse durations of 500 fs and 20 ps are adjusted with the grating compressor and measured with the help of a second order auto-correlator (APE) by fitting a temporal Gaussian profile and determining the full width at half maximum (FHWM) t_{ac} (see Fig. 3(a)). The short pulses of the CPA system with a FWHM duration of approximately 800 ps are measured using a 30 GHz Oscilloscope (LeCroy waveMaster 830Zi-A with 80 GS/s) (see Fig. 7(b)).

Additionally, the fusion process is studied at different repetition rates of 6 MHz, 10 MHz and 20 MHz, corresponding to pulse energies of 3.8 µJ, 2.5 µJ and 1.25 µJ, respectively. At an average power of 25 W, the pulse peak power in the presented experiments is extremely high in comparison to continuous illumination (25 W) with up to 10 MW for 500 fs and 5 kW for 800 ps, respectively.

Table 1
Overview of the applied laser parameters.

USP laser	Parameter	CW laser
1030 nm	Wavelength	1070 nm
50 µm	Spot diameter	50 µm
25 W	Average power	25 W
6–20 MHz	Repetition rate	–
500 fs–800 ps	Pulse duration	–

2.5. Sample analysis and preparation

The topography of fused walls and the impact on the powder bed has been measured using a laser scanning microscope (LSM700 by Zeiss) with a 10x objective yielding a resolution of 2.5 µm in each dimension.

For determining the shape and the size of the melt pool and characterizing the microstructure, the L-PBF samples were mounted in epoxy resin and ground with SiC papers up to a grit size of 1200, followed by polishing using 9 µm, 3 µm and 1 µm diamond suspensions and finally a suspension of 50 nm colloidal silica. The polished samples were etched using 1 g NaOH + 100 ml H_2O for up to 10 min. After etching, the microstructure was analyzed using an optical microscope (OM, Zeiss AXIO) and a scanning electron microscope (SEM, Zeiss Evo 40) equipped with a BSE detector and energy dispersive X-ray spectroscopy (EDX).

Porosity was characterized by X-ray computed tomography (CT). The micro-CT from phoenix|x-ray Systems uses a cone beam arrangement with a nanofocus x-ray tube. The $5 \times 5 \times 5$ mm^3 samples have been fixed on a polystyrene foam. 720 angles were recorded for a full turn using an integration time of 2 s and applying a voltage of 50 kV and current of 275 µA. The achieved voxel size was 3.8 µm in each dimension.

The image processing to analyze the porosity as well as the primary Si particles by the micrographs was realized using ImageJ and Matlab. Regarding the sufficient contrast of the images, a binarization is computed from the grey-scale histogram, setting the threshold to the dip between the two distinct broad peaks [40]. Additionally, the particle analysis tool of ImageJ has been used for determining the spatial distribution and average size of the primary Si.

Correlations between the microstructural features and the mechanical properties were studied using hardness tests. On the one hand the Vickers hardness is measured using a micro-hardness testing machine by Shimadzu and on the other hand the macro-hardness tests are conducted using a Brinell hardness testing machine by WPM. The Vickers hardness test is performed using a diamond pyramid with an angle of 136° that is pressed with a load of 0.2 kgf for 10 s into the polished surface of the samples. By contrast, during the Brinell hardness test an indenter ball made of tungsten with a diameter of 2.5 mm was pressed with a load of 62.5 kgf into a milled surface for 15 s (in accordance with ASTM E10; ISO 6506). For statistical significance, the indentation was repeated for 10 different positions on every sample.

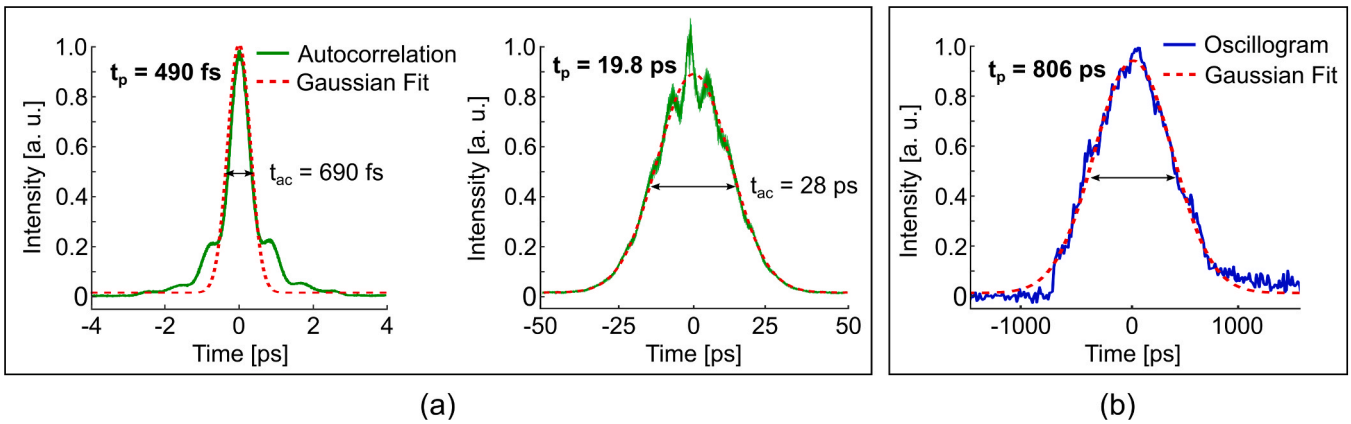

Fig. 3. Autocorrelation traces of the ultra-short laser pulses (a). The calculated FWHM pulse duration is $t_p = t_{ac}/\sqrt{2}$ [39] (a). Oscillogram of the stretched pulses of the CPA system measured using a 30 GHz oscilloscope and an InGaAs photodiode with a rise time of 12 ps.

3. Results and discussion

3.1. Limits of heat accumulation using ultra-short laser pulses

During the L-PBF process, the laser pulses may cause strong vaporization and ejection of particles/droplets, which should be avoided or kept to a minimum. For determining the damage threshold for single pulses, preliminary experiments were performed on a polished surface of an additively manufactured Al-40Si bulk sample. The method is based on the relationship between the diameter of the ablated crater D and the laser peak fluence $F_0 = \frac{8\,E_p}{\pi\,d_S^2}$ as given by Eq. 3:

$$D^2 = 0.5\,d_S^2\,\ln\left(\frac{F_0}{F_{th}}\right) \tag{3}$$

Then, the threshold fluence F_{th} can be obtained by linear extrapolation [41]. In Table 2, the threshold fluences for focused pulses with a diameter of 50 μm are compared to measurements on pure Al/Si sheets of a thickness of 1 mm.

The damage threshold for all the materials increases with increasing pulse duration, which is consistent with previous studies [42]. Due to the non-linear multiphoton absorption, the threshold for Si is higher than that for Al, approaching twice that of Al for a pulse duration of 800 ps. In comparison with pureAl/Si, the threshold fluences for Al-40Si are governed by the fraction of Al in the alloy. Concerning the spot diameter of 50 μm, the threshold for material damage starts at a pulse energy of 1.27 μJ at 500 fs, 1.57 μJ at 20 ps and 3.5 μJ at 800 ps. These values serve as a rough orientation for the onset of ablation effects during PBF. It should be noted that the damage threshold is reduced by multiple pulse irradiation, which is reported as an incubation or accumulation of plastic deformation resulting from thermal stress fields [43].

Based on these results, the feasibility for L-PBF at different repetition rates using Al-40Si powder was studied at the shortest pulse duration of 500 fs. According to previous investigations [10], a base of homogeneously molten single walls was produced at the beginning. A repetition rate of 20 MHz, an average power of 25 W, a scan speed v of 200 mm/s and a layer height of 15 μm are used in this step until the height of the base reaches 1 mm. Afterwards, the height of the powder layer is adjusted to 30 μm to cover the entire walls. On this powder layer, L-PBF at different repetition rates and pulse energies are tested. The top views of the final fused layers applying the same pulse overlap are shown in Fig. 4(a). The surrounding powder was colored in red to highlight the boundaries of the single walls.

Table 2
Single pulse threshold fluences in J/cm^2 of Al, Si and Al-40Si.

	Al	Si	Al-40Si
500 fs	0.11 ± 0.02	0.18 ± 0.03	0.13 ± 0.03
20 ps	0.15 ± 0.03	0.24 ± 0.03	0.16 ± 0.03
800 ps	0.31 ± 0.04	0.59 ± 0.06	0.36 ± 0.11

In all cases the pulse energy is 1 μJ, which is below the single pulse damage threshold. Additionally, the applied energy per unit length $E_S = P_{av}/v$ is 100 J/m. Complete melting only occurs at 20 MHz and 20 W. Balling effects are observed down to a repetition rate of 2 MHz, whereas at 1 MHz only weakly sintered particles are connected to the underlying wall. Here, the heat accumulation plays an important role for a stable melting process. It is reported, that bulk surface melting of metals induced by femtosecond laser pulses potentially starts at high repetition rates of 1 MHz for steel and 4 MHz for copper [44], respectively depending on the characteristic thermal diffusion length, l_{diff}, [45] given by Eq. 4:

$$l_{\mathrm{diff}} = \sqrt{4\,\alpha\,\Delta t} = \sqrt{\frac{4\,\alpha}{f_{\mathrm{rep}}}} \tag{4}$$

with the time span $\Delta t = f_{rep}^{-1}$ between two pulses, and the thermal diffusivity $\alpha = \frac{\kappa}{\rho\,C_p}$. Using the thermal conductivity $\kappa = 135$ W/m K [21], density $\rho = 2.54$ g/cm^3 [21] and specific heat capacity $C_p = 824$ J/kg K (rule of mixture) of Al-40Si the thermal diffusion length is 3 μm at 20 MHz and already 16 μm at 1 MHz. As a result, at higher repetition rates the heat is stored closer to the surface and within the focal volume before the next pulse arrives, i.e. it can be efficiently accumulated by the subsequent pulses. However, due to the extremely low thermal conductivity of the powder material, i.e. 0.2–1 W/m K [46,47], the heat is constrained inside the irradiated powder particles for a much longer time than in consolidated or bulk materials. Nevertheless, heat dissipation by conduction through sintered contact points, prevents a stable melting process at lower repetition rates.

In contrast to that, Fig. 4(b) shows the resulting walls produced using a constant average power of 12 W and a scan speed of 60 mm/s (200 J/m) at different repetition rates. In this case, the pulse energy reciprocally increases with decreasing repetition rate. Melting of the powder starts at a repetition rate of 5 MHz. However, with further decrease of the repetition rate to 2 MHz and the corresponding pulse energy of 6 μJ, ablation governs the L-PBF process and generates deep grooves in the center of the wall. This also leads to a strong removal of the powder close to the melting track, as can be seen from the profiles of the fused walls in Fig. 4(c), directly associated to the walls in Fig. 4(b). The supplied powder layers and fused walls are highlighted with red dashed lines and blue strips, respectively. The removal of powder particles at high pulse energies of 6 and 12 μJ in lateral and vertical directions can extend up to 100 μm, due to the induced shockwaves and recoil pressure, which prevents the production of solid bodies by fusing neighboring tracks.

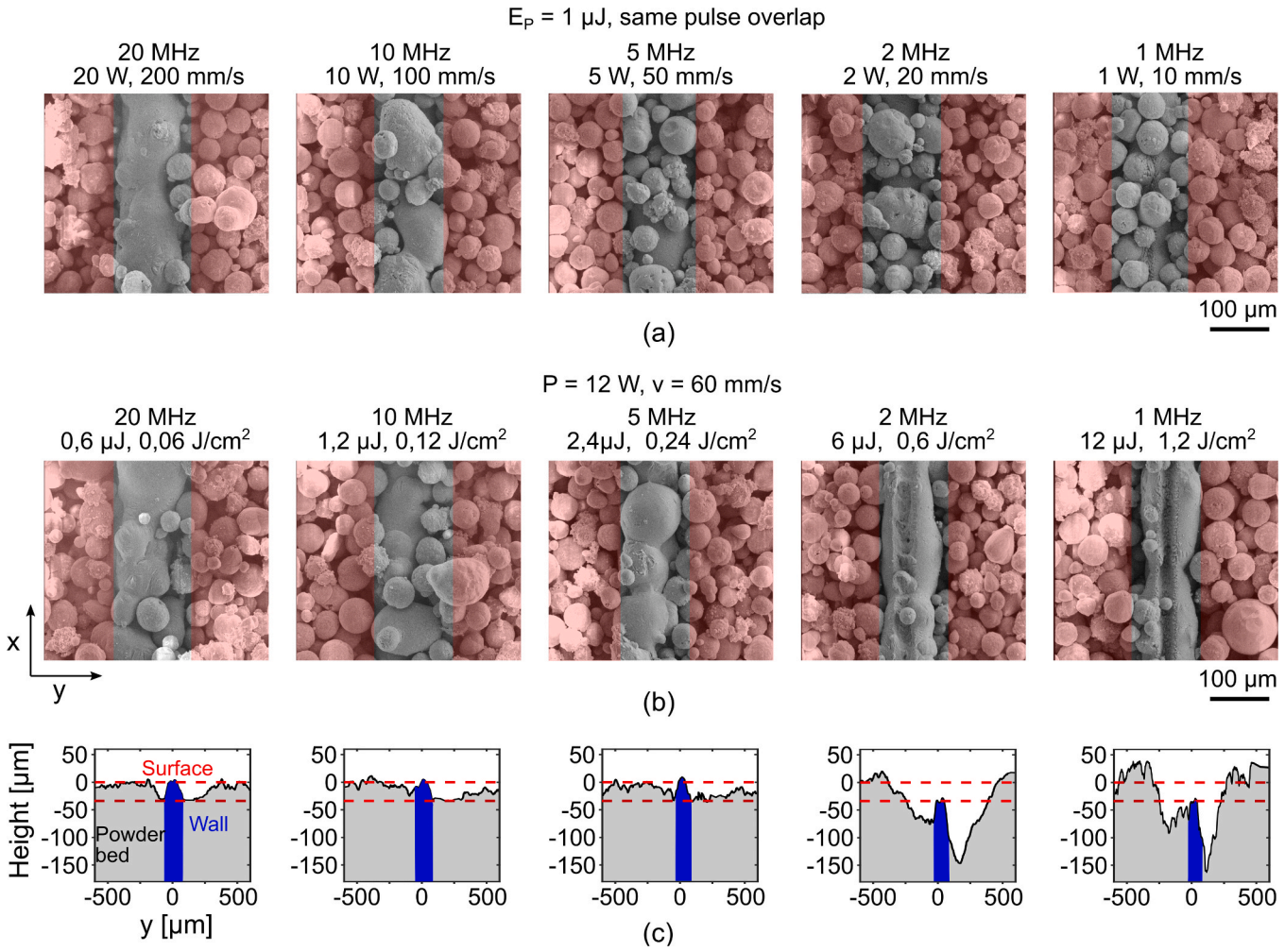

Fig. 4. SEM images of the last fused powder layer (top view). The single tracks are produced using 500 fs pulses and different repetition rates in the case of the same pulse energy of 1 µJ and the same pulse overlap (a) and in the case of the same applied average power of 12 W (b). The mean deviation of the as built surface along the scan direction together with the surrounding powder bed for (b) was measured using a laser scanning microscope (c). The profile lines represent an average value of all lines along the scan direction.

This blasting effect is reported for Al-40Si powder at a critical pulse fluence of 0.4 J/cm^2 using a beam diameter of 50 µm [10]. Despite of the high peak fluence of 0.24 J/cm^2 at 5 MHz, which is double that of the damage threshold for single pulses, no significant ablation or powder removal is observed. This could be explained by the fact, that the material ablation and removal become inefficient at higher repetition rates [44].

3.2. Melt pool geometry

According to these results and the studies reported in [10,18], L-PPF of single walls at an average power of 25 W has been performed to study the melt pool characteristics, starting with a repetition rate of 20 MHz. In Fig. 5(a) the top view of fused walls with a total height of 4 mm using a scan speed of 200 mm/s and a layer height of 15 µm are shown for different pulse modes in comparison to cw. With increasing pulse duration, the melt pool width increases combined with a reduced uniformity along the scanned path. As can be seen in Fig. 5(b), the melt pool widths are systematically lower at shorter pulse durations, even at different scan speeds. The smallest melt pool width of 70 µm was found at 500 fs and 250 mm/s, whereas the cw excitation leads to a distinctly larger minimum width of 105 µm at the same scan speed. The width of the melt pool significantly increases with the pulse duration increasing from 20 ps to 800 ps and then to cw. With the pulse duration decreasing from 20 ps to 500 fs, the difference in the width of the melt pool is only obvious at high scan speeds above 200 mm/s.

To estimate the depth of the melt pool, the microstructure of the produced wall along the build direction was characterized, as shown in Fig. 5(c). In the melt pool area at the tip of the wall (marked in red), the primary Si phase (black) is fine and distributed homogeneously. Underneath the melt pool, the Si phase is coarser due to the thermal treatment after every single fused layer in the heat affected zone (HAZ), as illustrated in light yellow. In contrast to the width W, the melt pool depth D increases with decreasing pulse duration. The aspect ratio between depth and width $AR = D/W$ of the melt pool is shown in Fig. 5(d). For cw, AR is almost independent of the scan speed, with the lowest values around 0.37. For the L-PBF using short pulses, the influence of the scan speed on AR is more pronounced and becomes higher with decreasing pulse duration with values of about 0.5 at 500 fs and 100 mm/s. In combination with the typical semi-circular melt pool shape, the AR indicates that the melt pool is mainly controlled by thermal conduction [48] as predicted by the conduction-mode model [49], where the depth is nearly half of the width that is also referred by Weckman et al. [50] at values below 0.5. Nevertheless, the deeper but thinner melt pool at higher peak intensities for 500 fs and 20 ps pulses with lower scan speeds suggests the occurrence of stronger vaporization, indicating the onset of keyhole melting [48]. The threshold speed v_{th} for this mode has already been studied and experimentally proven in L-PBF

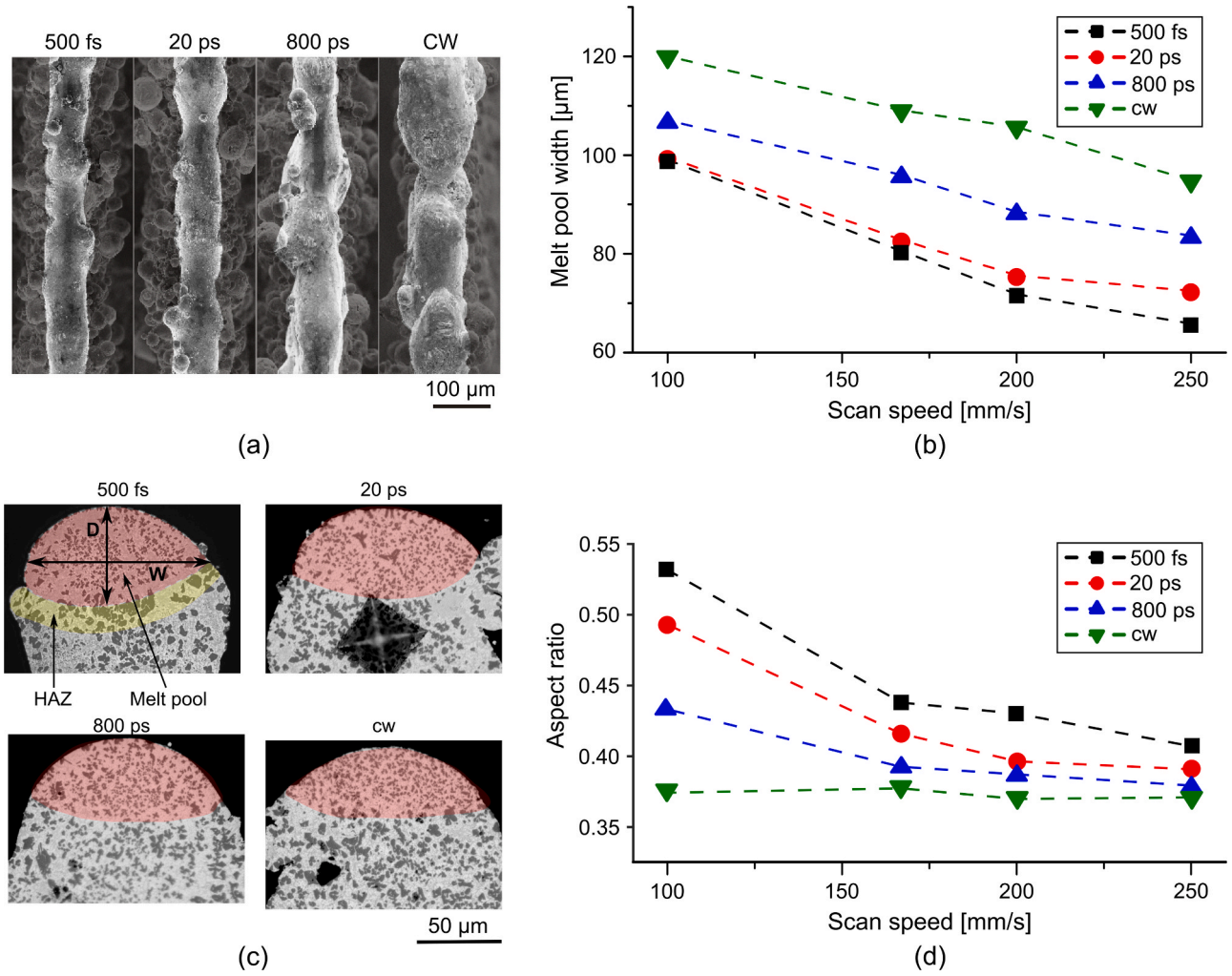

Fig. 5. SEM images of walls (top view) produced at a repetition rate of 20 MHz, a scan speed of 200 mm/s, and a layer height of 15 µm (a). (b) Graphical representation of the melt pool width depending on scan speed and pulse duration at a repetition rate of 20 MHz. (c) The melt pool width (W) was determined by the microstructural change at the tip of the walls captured by OM. (d) The estimated aspect ratio between the melt pool depth (D) and width (W) shows an increase at shorter pulse durations.

of 316L stainless steel [51] and Al7050 [48] and is given by Eq. 5:

$$v_{th} = \frac{4\,\alpha}{d_S}\left[\frac{\sqrt{\pi}\;\kappa\,T_B}{\eta\,I_0\,d_S}\right]^{-2}, \tag{5}$$

where, T_B is the boiling point (2743 K for Al and 3533 K for Si [52]) of the material and η (0.5) the laser absorptivity, which was measured during powder melting using an integrating sphere. The threshold scan speed is calculated to be between 30 mm/s (based on T_B of Si) and 50 mm/s (based on T_B of Al). Since these values are lower than those in the present investigation, the *AR* is supposed to be influenced by the high peak intensities of the applied pulses. As mentioned in Section 3.1, the single pulse damage or ablation threshold for 500 fs is 1.27 µJ, which is close to the pulse energy of 1.25 µJ used in this experiment. Due to the reduction of the threshold by incubation, this energy level could lead to an evaporation rate which is suitable to deeply dent the melt pool by recoil forces, resulting in a transition to keyhole melting.

3.3. Keyhole melting

Applying the same average power, a reduction of the repetition rate and/or the pulse duration will lead to higher applied peak intensities. As can be seen in Fig. 6(a), using lower repetition rates (higher pulse energies) the melt pool width is increased and the homogeneity of the fused walls is enhanced. Even if the relaxation time between two successive pulses is doubled, the melt pool width at 500 fs is increased by more than 30% by a change from 20 MHz to 10 MHz or 1.25 µJ to 2.5 µJ in pulse energy, respectively (see Fig. 6(b)) and exceeds the average value at cw. A further increase of the pulse energy (or decrease in the repetition rate) is not feasible at 500 fs and 20 ps due to the strong removal of the powder particles as can be seen in the profile cross-section in the bottom left of Fig. 6(a). However, at 800 ps the peak power is more than three orders of magnitudes lower than at 500 fs and a stable L-PBF process with negligible powder bed distortions is achieved at 6 MHz and 3.8 µJ (0.39 J/cm^2). A profound change in the melt pool width only becomes apparent at this energy level (bottom right in Fig. 6(a) and (b)) with an increase of more than 20% of the melt pool width at 100 mm/s in contrast to 20 MHz and 10 MHz.

The melt pool boundaries at 500 fs and 10 MHz exhibit a V-shape on the bottom as shown in Fig. 6(c), which is characteristic for the keyhole melting mode [48]. In these cases, the applied peak intensities of more than $5{\cdot}10^{11}$ W/cm^2 at 500 fs are high enough to allow extensive vaporization during L-PBF, where the recoil pressure exceeds the hydrostatic pressure and surface tension of the liquefied metal resulting in a deeper melt pool penetration [53]. Furthermore, a higher portion of the applied laser energy is absorbed by the increased area of the deformed surface and by multiple reflections on the keyhole wall, that additionally reduce the threshold intensity for this melting mode. The

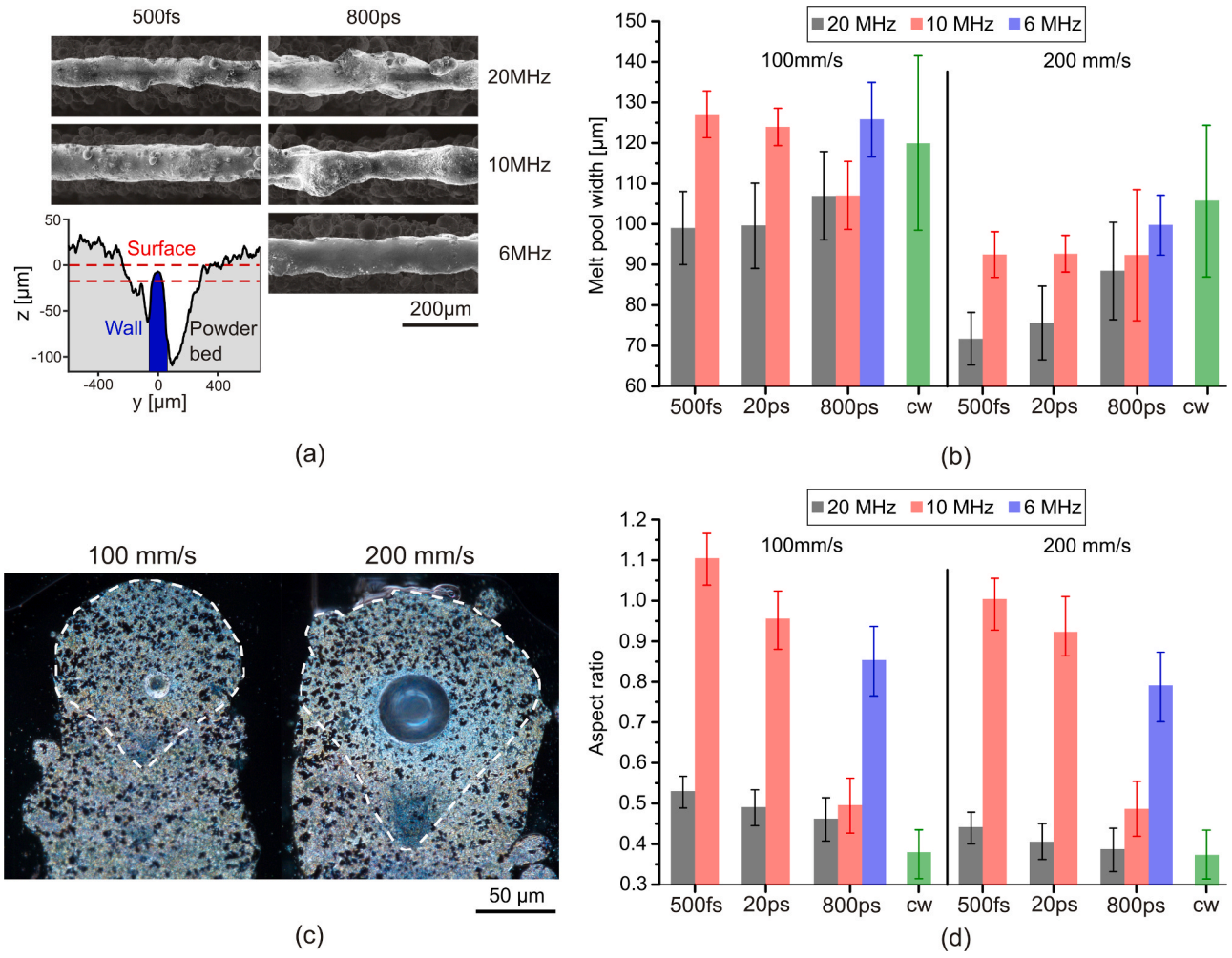

Fig. 6. SEM images of walls (top view) generated at a scan speed of 200 mm/s (a). The graph in the bottom left shows a profile of the distorted powder bed after the interaction with high energetic pulses at 500 fs and 6 MHz. (b) Variation of the melt pool widths at different repetition rates using scan speeds of 200 mm/s and 100 mm/s, respectively. (c) Polished cross-sections of two walls produced using 500 fs with a repetition rate of 10 MHz. The melt pool boundaries are illustrated by the dashed white outlines. (d) Melt pool aspect ratio at different repetition rates using scan speeds of 200 mm/s and 100 mm/s.

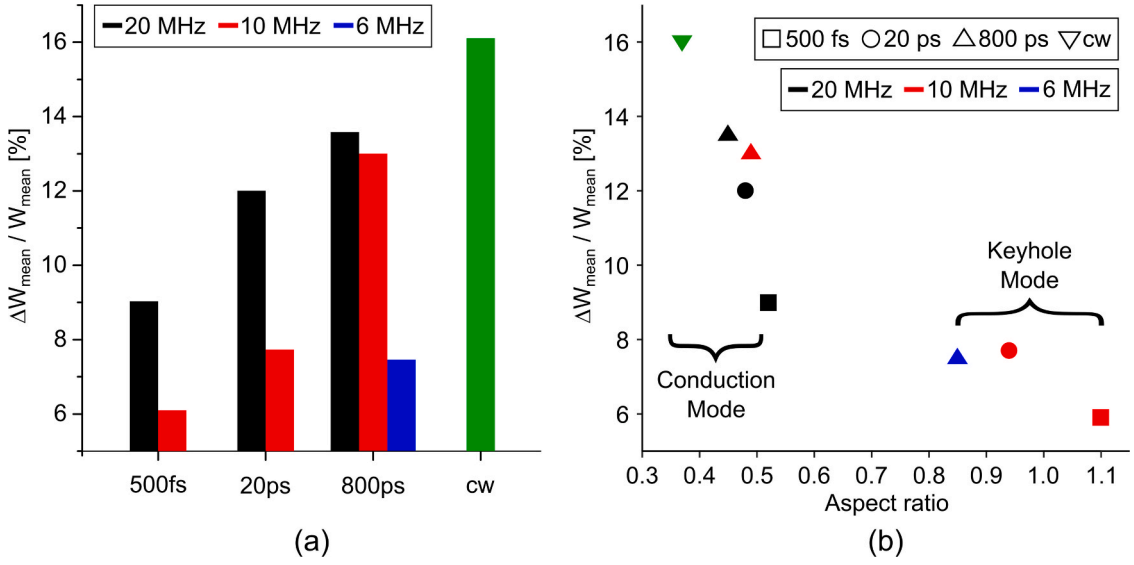

Fig. 7. Relative deviation of the melt pool width $\Delta W_{mean}/W_{mean}$ at a scan speed of 100 mm/s in dependence on the pulse duration and repetition rate (a) as well as the melt pool aspect ratio (b).

AR's obtained at 500 fs and 20 ps using 10 MHz (2.5 μJ) increase to around unity in comparison to that at 20 MHz (1.5 μJ), as well as for 800 ps at 6 MHz (3.8 μJ), as shown in Fig. 6(d). Hence, the transition to keyhole melting sets on, if the particular laser pulse fluence exceeds the single pulse ablation threshold. Therefore, the average intensity I_0 used for the threshold evaluation plays a rather subordinate role.

According to Figs. 5(a) and 6(a) the track shapes of the solidified walls and consequently their waviness and roughness strongly depending on the used pulse duration and repetition rate. Fig. 7(a) shows the relative deviation of the melt pool mean width $\Delta W_{mean}/W_{mean}$ along the scanned path (top view) as a measure for the shape accuracy depending on the pulse mode. The $\Delta W_{mean}/W_{mean}$ values are systematically lower at decreasing pulse durations, which corresponds to a higher uniformity of the wall shapes. In addition, a continuous increase of the uniformity (decrease of $\Delta W_{mean}/W_{mean}$) is observed at the transition from conduction to keyhole melting at 10 MHz for ultra-short laser pulses and 6 MHz for 800 ps by correlating $\Delta W_{mean}/W_{mean}$ with the *AR* of the melt pool as shown in Fig. 7(b). In contrast to that, cw processing with the lowest *AR* shows an enhanced local necking, balling effects and more pronounced surface irregularities, which can also be observed - to a lesser extent - at 800 ps and 20 MHz.

3.4. Keyhole porosity

Although the shape of the walls in this keyhole regime at lower repetition rates is more uniform combined with less sintered particles at the wall edges, the formation of a vapor channel can lead to an incomplete collapse of the resulting cavities, that leaves voids behind [53], which can be observed in the central parts of the melt pools in Fig. 6(c). The influence of the melting mode on this effect is shown in Fig. 8 at cross-sections of walls produced using a scan speed of 100 mm/s.

At 20 MHz all the walls contain a few micron- and submicron-sized pores independent of the pulse duration. It is reported that these pores result from hydrogen, that is released during the evaporation of the moisture content at the powder particle surface and the dissolved hydrogen in Al during L-PBF [54]. At lower repetition rates and the transition from conduction to keyhole melting, the number and size of the pores is increasing depending on the applied pulse duration with a strongly reduced void density of 0.54% at 500 fs up to 7.8% at 800 ps (see Table 3). Furthermore, L-PBF at 6 MHz and 800 ps leads to a pronounced chain-like void structure in the central area along the build direction. Consequently, the collapsing of the cavities during solidification is more efficient in the ultra-short pulsed regime. One possible reason for this effect could be the generation of stronger acoustic shockwaves that additionally drive the gas inclusions towards the surface, which is in good agreement with studies reported by Zhao et al. [55] and Kuo et al. for pulsed laser welding [56].

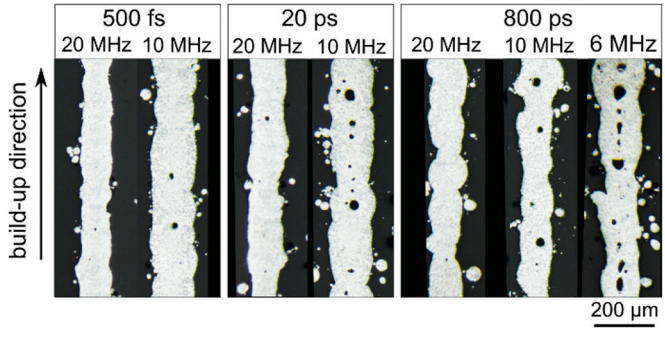

Fig. 8. OM images of polished walls along the build direction, generated using a scan speed of 100 mm/s.

Table 3
Area density of the voids in dependence on the laser parameters and melting mode estimated from the cross-section images of Fig. 8.

Pulse mode	Melting Mode	Void porosity [%]
500 fs, 20 MHz, 1.25 μJ	"Transition"	0.05 ± 0.02
500 fs, 10 MHz, 2.5 μJ	Keyhole	0.54 ± 0.05
20 ps, 20 MHz, 1.25 μJ	Conduction	0.24 ± 0.03
20 ps, 10 MHz, 2.5 μJ	Keyhole	3.5 ± 0.1
800 ps, 20 MHz, 1.25 μJ	Conduction	0.05 ± 0.01
800 ps, 10 MHz, 2.5 μJ	"Transition"	2.9 ± 0.1
800 ps, 6 MHz, 3.8 μJ	Keyhole	7.8 ± 0.3

3.5. Microstructure of L-PBF Al-40Si

According to the Al-Si phase diagram [22,57] (see Fig. 1(a)), the Si phase will precipitate from the melt first, followed by the formation of eutectic according to the reaction: liquid → α-Al + Si at 577 °C. In comparison to the coarse primary Si plates in the as-cast Al-40Si ingot, the primary Si phase (black in Fig. 9(a)) in the USP-L-PBF samples is much finer and exhibits spherical or dendritic morphology when observed by OM.

The primary Si becomes finer with decreasing pulse duration using the same scan speed of 167 mm/s at a repetition of 20 MHz. A layer of α-Al forms surrounding the primary Si phase due to the depletion of Si in the melt during the growth of primary Si. In BSE contrast at higher magnification, a mixture of α-Al (black in Fig. 9(b)) and Si (white) is observed between the primary Si. This mixture is composed of α-Al dendrites with interdendritic Si phase with a spacing of 350 ± 50 nm for the cw sample. For a pulse duration of 500fs, this mixture is characterized as ultra-fine eutectic with an approximated spacing of 110 ± 20 nm, which is also significantly finer than that from spray forming [24,58,59] or melt spinning [25,60]. The volume fraction of the Si phase in this fine eutectic structure is significantly higher than that in the as-cast ingot, leading to a mean Si concentration of 22 wt% measured using EDX. This is caused by much higher cooling rates during L-PBF, which is in the range of 10^3 to 10^6 K/s [61,62], and a high melt undercooling [63,64] when USPs are applied. EDX analysis confirmed nearly the same total Si content of approximately 39 ± 1 wt% for all the L-PFB samples, which indicates the negligible impact of the evaporation of Al and Si during the processes [65]. Based on Fig. 9(a) the volume fraction of the primary Si obtained by optical granulometry increases from 24 ± 2 vol% at 500 fs to 30 ± 3 vol% at 800 ps to 34 ± 3 vol% for cw. This indicates a higher volume fraction of the eutectic structure at shorter pulse durations, as can be deducted from Fig. 9(b). Due to the higher volume fraction of the primary Si phase in the cw sample, the melt surrounding the primary Si during solidification has a lower Si content, which promotes the precipitation of the α-Al phase as the primary phase in the melt between the primary Si crystals and thus the formation of α-Al dendrites.

The area of the cross-section of the melt pools is calculated by $A = \pi/4 \times W \times D$, which is approximately $(3 \pm 0.5) \times 10^3$ μm^2 in all operation modes for the used parameter set (see Fig. 9(c)). Assuming that the influence of comparable melt pool volumes on the cooling rate can be neglected and the keyhole effect has no particular significance, the characteristic length of the primary Si phase at the tip of walls was measured (based on Fig. 9(a)). The average length of the primary Si phase decreases from a mean value of 3 μm for cw irradiation down to 1.5 μm at 500 fs (see Fig. 9(c)). The refinement at shorter pulse durations can be attributed to the higher applied peak intensities, that induce larger thermal gradients and a stronger local melt overheating [66].

The melting mode has a significant influence on the solidification morphology as well. The microstructure of the cross-section of two walls produced at 500 fs is shown in Fig. 10 (a). The distribution of primary Si (dark) at 20 MHz shows an accumulation of larger particles in the center and at the edges. In contrast, after keyhole melting at 10 MHz the Si phase forms with significantly finer extension in the central area of the

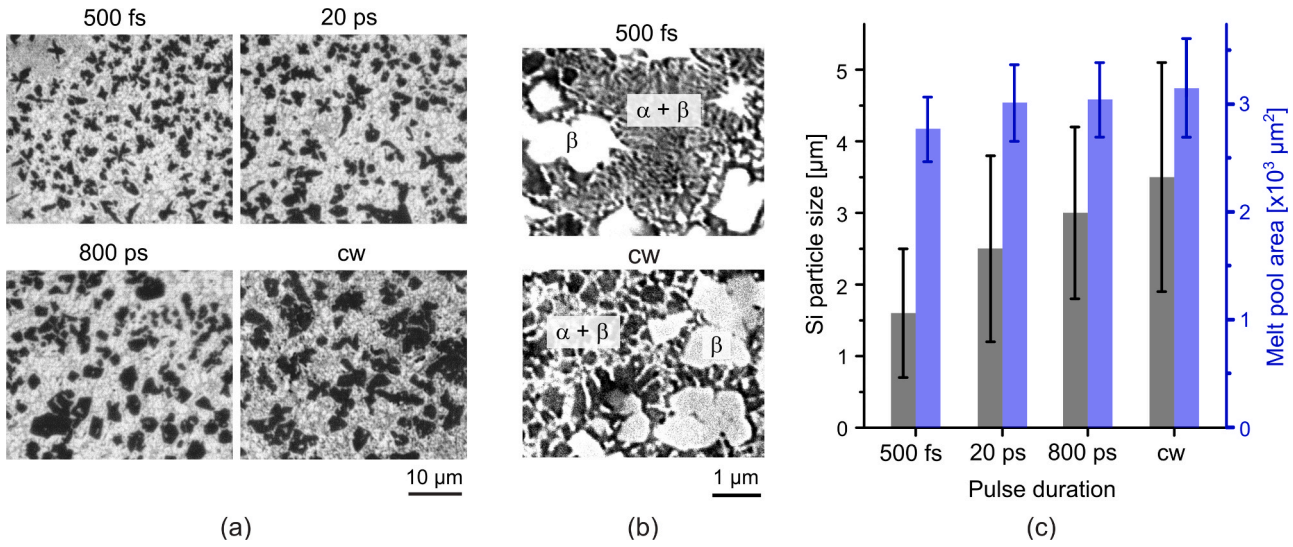

Fig. 9. (a) OM images of the fused walls using a repetition rate of 20 MHz and a scan speed of 167 mm/s. Si appears in black, and α-Al in white. (b) BSE images of the L-PBF samples at higher magnification, where the white phase is Si and the black is α-Al. (c) Mean size of the primary Si phase and the melt pool area depending on the pulse mode.

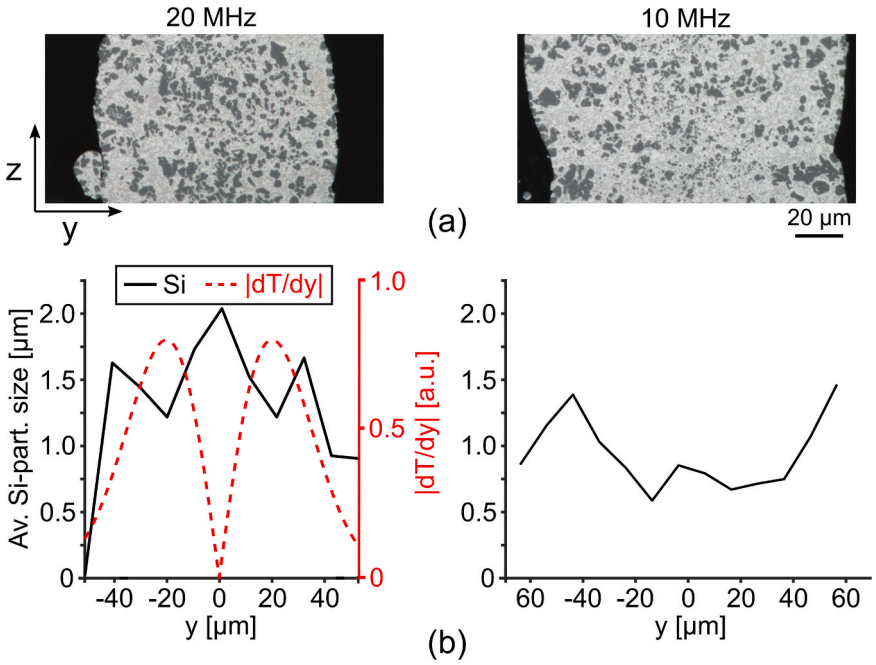

Fig. 10. OM images of cross-sections along the build direction showing the transition from conduction (20 MHz) to keyhole melting mode (10 MHz) at 500 fs and a scan speed of 200 mm/s (a). The average primary Si particle size along the y-direction obtained by the corresponding cross-sections plotted together with the expected absolute value of the thermal gradient (b).

wall, even though the melt pool is larger. The microstructure at the edges of the sample from 10 MHz is similar to that from 20 MHz. The size distribution of Si was analyzed by determining the average Si particle size (length) within separated areas of 10 × 10 µm^2. The average size of primary Si along the y-direction is shown in Fig. 10 (b).

The size of the primary Si phase for 20 MHz is mainly governed by the thermal gradient dT/dy (red dashed line in Fig. 10(b)), which is in a first approximation proportional to the absolute value of the first derivative of the temperature field induced by a moving point heat source $T(y) \sim \exp\left[-\frac{y^2}{4\alpha t}\right]$ [67] based on the heat conduction equation. As a simplified approach, it visualizes the inverse correlation with the size of the primary Si phase. Hence, the higher the thermal gradient, which sets the solidification front velocity and the cooling rate, the smaller the size of the primary Si phase, which is consistent with previous studies [68]. In contrast, the size distribution of the primary Si phase of the L-PBF sample processed in the keyhole melting mode exhibits a drop in the central part of the fused wall, which is influenced by the vapor channel. Due to the extremely high thermal gradient at the hot keyhole wall to the surrounding metal, the heat loss is very strong, where the bottom of the keyhole solidifies rapidly [69] resulting in a more pronounced refinement of the primary Si phase. Additionally, the temperature in the material close to the keyhole wall undergoes a melt overheating, which has a positive influence on the refinement [66], as mentioned before. At the edge of the fused wall, where the influence of the keyhole is significantly reduced, the size distribution of the primary Si is consistent

with that from the conduction mode, contributing to the comparable size of the primary Si phase in the two samples.

3.6. Microhardness

The refinement of the primary Si particles and of the eutectic structure is supposed to exhibit a positive influence on the mechanical properties [20,22,70]. As a first estimation, the microhardness was measured in the central area of the cross section of the fused walls produced using the scan speed of 200 mm/s. The Vickers hardness increases with deceasing pulse duration for both repetition rates of 10 and 20 MHz, as shown in Fig. 11. The samples produced with a pulse duration of 500 fs at the repetition rate of 20 MHz approaches 150 HV, and the one at 10 MHz is about 170 HV, which is more than 25% higher in comparison to cw (135 HV) and 50% higher than of the spray formed Al-42Si (110 HV), which serves as an industrial reference. Additionally, the observed refinement of the microstructure from the conduction (20 MHz) to the keyhole melting mode (10 MHz) in the central region is also reflected by an increase of the microhardness of more than 10% for all pulse durations.

3.7. Bulk properties

In order to analyze the performance of fused bulk samples, cubes with a size of 5 × 5 × 5 mm^3 were produced using an average power of 25 W, a scan speed of 200 mm/s, a hatch spacing s of 50 µm and layer height h of 15 µm, yielding the same volumetric energy density $VED = \frac{P}{v\,s\,h} = 167$ J/mm^3 for the different operation modes. Every layer was scanned line-by-line with the same pattern to ensure comparability. Representative slices from the samples produced using different pulse durations and repetition rates obtained by X-ray CT are shown in Fig. 12 (a). With a repetition rate of 20 MHz, a similar structure of the porosity and size distribution of pores are observed for the different pulse durations and cw, indicating its independency of the excitation mode. The main contribution to the porosity is a lack of fusion caused by insufficient heat penetration and wettability problems during the fusion process. In the (transition) keyhole mode at a repetition rate of 10 MHz in the pulsed regime, a significant densification with less porosity is achieved. With respect to the results of the previous sections, the enhanced energy coupling efficiency in the keyhole melting mode using 500 fs and 20 ps at 10 MHz leads to a higher densification up to relative densities of 94 ± 1% and 93 ± 1% in contrast to 800 ps with 89 ± 2%.

The Brinell hardness was measured for the samples produced at 20 MHz having a similar pore structure to emphasize the effect of the solidification morphology and is shown in Fig. 12 (b). It significantly increases from 105 HB for cw up to 155 HB in the USP-regime as a result of the significant refinement of the primary Si phase and of the surrounding fine eutectic and Si-enriched α-Al matrix at shorter pulse durations. After annealing at a temperature of 360 °C for 6 h to reduce thermally induced stresses, generated during the fusion process, the hardness is reduced due to the dissolution of the eutectic structure in the α-Al matrix and coarensing of the Si particles [20]. Nevertheless, for 500 fs the hardness is still 118 HB, which is higher than that of spray formed Al-42Si that has a relative density of more than 99%. It should be noted that this value is nearly twice the hardness of the as-cast Al-40Si sample of 66 HB (cf. Fig. 1(b)).

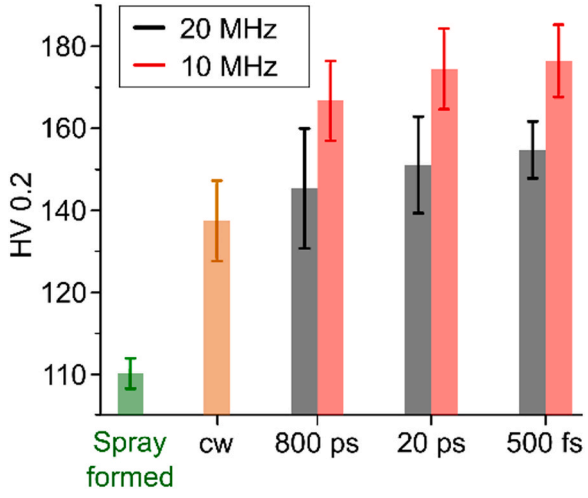

Fig. 11. Vickers hardness of the L-PBF samples at a scan speed of 200 mm/s depending on the pulse duration and repetition rate in comparison to cw processed and spray-formed samples depicted in Fig. 1(c).

4. Conclusion

Ultra-short laser pulses reveal an enormous potential as a heat source in high precision laser powder bed fusion of Al-Si alloys, allowing a reduced melt pool width and a stronger refinement of the microstructure. Due to heat dissipation by conduction losses, an average power and repetition rate of more than 10 W and 1 MHz, respectively is needed for generating a stable melt pool on a thin powder layer in the presented experimental configuration. The maximum applied pulse energy for L-PBF is limited to nearly twice the ablation threshold for single pulses. If the pulse fluence exceeds a critical value of 0.4 J/cm^2 extensive powder removal and ablation is taking place. In a comprehensive investigation using different pulse durations ranging from the ultra-short range at 500 fs to the short pulse regime at 800 ps in comparison to a continuous wave laser at an average power of 25 W and using a spot diameter of 50 µm, we can draw the following conclusions:

1. L-PBF using ultra-short laser pulses at 500 fs and 20 ps show a reduction of the melt pool widths to a minimum size of 70 µm at 20 MHz and a significantly higher shape accuracy as compared to cw.
2. At pulse energies higher than the single pulse ablation threshold, vaporization leads to the transition from conduction to keyholes melting, enabling higher melt penetration depths. Using ultra-short laser pulses melt pool aspect ratios of around unity are observed in contrast to 0.37 using cw radiation.
3. The void porosity in the keyhole melting mode is significantly reduced using 500 fs laser pulses, enabling the use of this mode for L-PBF.
4. An enhanced refinement of the primary Si phase and eutectic structure is observed using ultra-short laser pulses. This results in an increased microhardness, that is distinctly higher in comparison to cw and other rapid solidification techniques such as spray forming.
5. The relative density of the produced bulk specimen is increased at higher pulse energies and shorter pulse durations and is significantly higher in comparison to cw.

In future work, we will focus on the implementation of pump-probe experiments to clarify fundamental aspects of the interaction of ultra-short laser pulses with the generated plasma, vapor and smoke during laser powder bed fusion. Additionally, the determination of the material properties, such as the ultimate tensile strength, Young's modulus and the coefficient of thermal expansion of hypereutectic Al-Si alloys will be carried out. This data will be important to address new fields of applications in astronomy, automotive and electronic industry.

CRediT authorship contribution statement

Tobias Ullsperger: Conceptualization, Investigation, Methodology, Formal analysis, Writing - original draft. **Dongmei Liu:** Investigation, Writing - review & editing. **Burak Yürekli:** Writing - review & editing. **Gabor Matthäus:** Supervision, Funding acquisition. **Lisa Schade:**

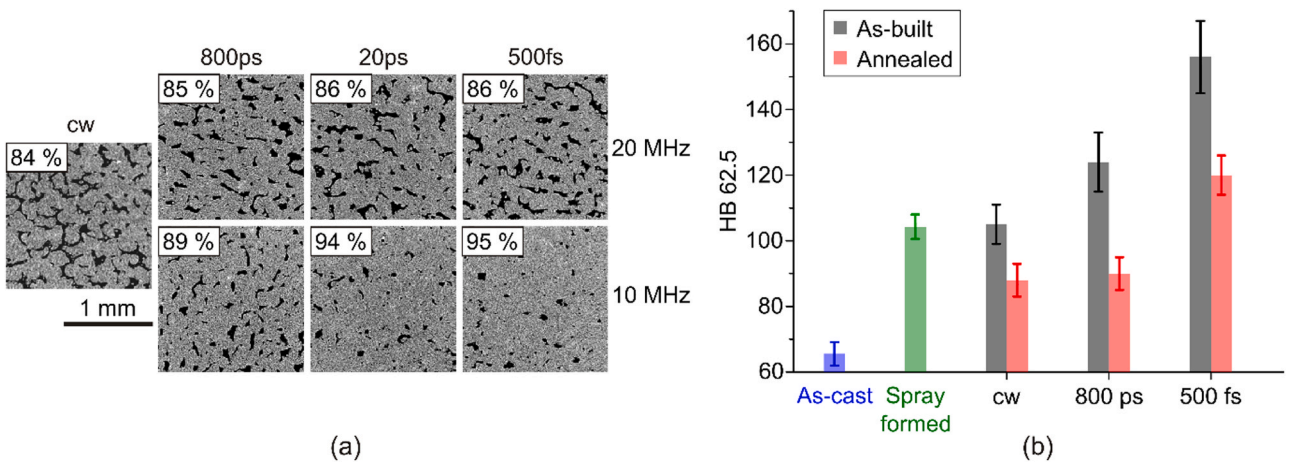

Fig. 12. X-ray CT slices of the bulk samples along the build direction (a). The corresponding relative densities are shown in the top left. (b) shows a graphical representation of the Brinell hardness of the samples produced at 20 MHz and 200 mm/s depending on the pulse duration in comparison to cw. For comparison the Brinell hardness of the rapidly solidified, spray-formed specimen as well as the as-cast sample shown in Fig. 1(b) is included.

Writing - review & editing. **Brian Seyfarth:** Writing - review & editing. **Hagen Kohl:** Writing - review & editing. **Roland Ramm:** Investigation, Resources. **Markus Rettenmayr:** Project administration, Funding acquisition, Writing - review & editing. **Stefan Nolte:** Project administration, Funding acquisition, Supervision, Writing - review & editing.

Declaration of Competing Interest

The authors declare that they have no known competing financial interests or personal relationships that could have appeared to influence the work reported in this paper.

Acknowledgments

We gratefully acknowledge support by the German Research Foundation (DFG) within the Priority Program (SPP) 2122 “Materials for Additive Manufacturing (MATframe)” (NO462/13-1 and RE1261/23-1) and the German Federal Ministry of Education and Research (BMBF) within the project AM-OPTICS (02P15B203). Lisa Schade acknowledges support by TRUMPF Laser GmbH. Brian Seyfarth likes to acknowledge the Center of Excellence in Photonics of the Fraunhofer Institute for Applied Optics and Precision Engineering (IOF). Furthermore, we would like to thank Johannes Wilke from the Otto Schott Institute of Material Research for the metallographic work and Marco Müller from the Fraunhofer IOF for producing the cw reference samples on the commercial L-PBF machine.

References

[1] E.O. Olakanmi, R.F. Cochrane, K.W. Dalgarno, Progress in material, a review on selective laser sintering/melting (SLS/SLM) of aluminium alloy powders: processing, microstructure, and properties, Prog. Mater. Sci. 74 (2015) 401–477, https://doi.org/10.1016/j.pmatsci.2015.03.002.

[2] D. Buchbinder, H. Schleifenbaum, S. Heidrich, W. Meiners, J. Bültmann, High power selective laser melting (HP SLM) of aluminum parts, Phys. Procedia 12 (2011) 271–278, https://doi.org/10.1016/j.phpro.2011.03.035.

[3] R. Glardon, N. Karapatis, V. Romano, G.N. Levy, Influence of Nd:YAG parameters on the selective laser sintering of metallic powders, CIRP Ann. 50 (1) (2001) 133–136, https://doi.org/10.1016/S0007-8506(07)62088-5.

[4] J.-P. Kruth, X. Wang, T. Laoui, L. Froyen, Lasers and materials in selective laser sintering, Assem. Autom. 23 (2003) 357–371, https://doi.org/10.1108/01445150310698652.

[5] R. Ebert, F. Ullmann, D. Hildebrandt, J. Schille, L. Hartwig, S. Kloetzer, A. Streek, H. Exner, Laser processing of tungsten powder with femtosecond laser radiation, J. Laser Micro/Nanoeng. 7 (1) (2012) 38–43, in: https://www.researchgate.net/publication/259331694_Laser_Processing_of_Tungsten_Powder_with_Femtosecond_Laser_Radiation/link/53d8fc8c0cf2a19eee83a352/download.

[6] R. Ebert, F. Ullmann, J. Schille, U. Loeschner, H. Exner, Investigation of cw and ultrashort pulse laser irradiation of powder surfaces - a comparative study, Proceedings of SPIE 8607, 2013, 86070X. https://doi.org/10.1117/12.2006406.

[7] B. Nie, H. Huang, S. Bai, J. Liu, Femtosecond laser melting and resolidifying of high-temperature powder materials, Appl. Phys. A 118 (1) (2015) 37–41, https://doi.org/10.1007/s00339-014-8897-y.

[8] B. Nie, L. Yang, H. Huang, S. Bai, P. Wan, J. Liu, Femtosecond laser additive manufacturing of iron and tungsten parts, Appl. Phys. A 119 (3) (2015) 1075–1080, https://doi.org/10.1007/s00339-015-9070-y.

[9] L. Kaden, G. Matthäus, T. Ullsperger, H. Engelhardt, M. Rettenmayr, A. Tünnermann, S. Nolte, Selective laser melting of copper using ultrashort laser pulses, Appl. Phys. A 123 (596) (2017), https://doi.org/10.1007/s00339-017-1189-6.

[10] T. Ullsperger, G. Matthäus, L. Kaden, H. Engelhardt, M. Rettenmayr, S. Risse, A. Tünnermann, S. Nolte, Selective laser melting of hypereutectic Al-Si40-powder using ultra-short laser pulses, Appl. Phys. A 123 (798) (2017), https://doi.org/10.1007/s00339-017-1337-z.

[11] B.N. Chichkov, C. Momma, S. Nolte, F. von Alvensleben, A. Tünnermann, Femtosecond, picosecond and nanosecond laser ablation of solids, Appl. Phys. A 63 (2) (1996) 109–115, https://doi.org/10.1007/BF01567637.

[12] C. Momma, S. Nolte, B.N. Chichkov, F. von Alvensleben, A. Tünnermann, Precise laser ablation with ultrashort pulses, Appl. Surf. Sci. 109–110 (1997) 15–19, https://doi.org/10.1016/S0169-4332(96)00613-7.

[13] F. Bauer, A. Michalowski, S. Nolte, Residual heat in ultra-short pulsed laser ablation of metals, J. Laser Micro /Nanoeng. 10 (3) (2015) 325–328, https://doi.org/10.2961/jlmn.2015.03.0016.

[14] R. Weber, T. Graf, P. Berger, V. Onuseit, M. Wiedenmann, C. Freitag, A. Feuer, Heat accumulation during pulsed laser materials processing, Opt. Express 22 (9) (2014) 11312–11324, https://doi.org/10.1364/OE.22.011312.

[15] E.G. Gamaly, A.V. Rode, B. Luther-Davies, Ultrafast ablation with high-pulse-rate lasers. Part I: theoretical considerations, J. Appl. Phys. 85 (8) (1999) 4213–4221, https://doi.org/10.1063/1.370333.

[16] S.M. Eaton, H. Zhang, P.R. Herman, F. Yoshino, L. Shah, J. Bovatsek, A.Y. Arai, Heat accumulation effects in femtosecond laser-written waveguides with variable repetition rate, Opt. Express 13 (12) (2005) 4708–4716, https://doi.org/10.1364/OPEX.13.004708.

[17] S. Richter, S. Döring, A. Tünnermann, S. Nolte, Bonding of glass with femtosecond laser pulses at high repetition rates, Appl. Phys. A 103 (2) (2011) 257–261, https://doi.org/10.1007/s00339-011-6369-1.

[18] T. Ullsperger, G. Matthäus, L. Kaden, B. Seyfarth, H. Engelhardt, D. Liu, M. Rettenmayr, S. Nolte, Optimization of mechanical properties and as-built quality of additive manufactured Al-Si alloys using ultra-short laser pulses, Lasers in Manufacturing (LiM), Munich, Germany, 2019. https://www.wlt.de/lim/Proceedings2019/data/8.html.

[19] E. Hilpert, J. Hartung, H. von Lukowicz, T. Herffurth, N. Heidler, Design, additive manufacturing, processing, and characterization of metal mirror made of aluminum silicon alloy for space applications, Opt. Eng. 58 (9) (2019) 1, https://doi.org/10.1117/1.OE.58.9.092613.

[20] M. Mueller, M. Riede, S. Eberle, A. Reutlinger, A.D. Brandão, L. Pambaguian, A. Seidel, E. López, F. Brueckner, E. Beyer, C. Leyens, Microstructural, mechanical, and thermophysical characterization of hypereutectic AlSi40 fabricated by selective laser melting, J. Laser Appl. 31 (2) (2019), 022321, https://doi.org/10.2351/1.5096131.

[21] “RSP Technology: RS Alloys Optics,” [Online]. Available: http://www.rsp-technology.com/site-media/user-uploads/rsp_alloys_optics_2018lr.pdf, Accessed on: 8 February 2021.

[22] E. Hilpert, S. Risse, Materials Science & Technology Conference and Exhibition MS&T'15, Columbus, Ohio, 4–8 October 2015 (Association for Iron & Steel Technology, Warrendale, PA, 2015).

[23] J.L. Murray, A.J. McAlister, The Al-Si (Aluminum-Silicon) system, Bull. Alloy Phase Diagr. 5 (1) (1984) 74–84, https://doi.org/10.1007/BF02868729.

[24] W. Kahl, J. Leupp, Spray deposition of high performance aluminium alloys via the Osprey process, Swiss Mater. 2 (17) (1990).

[25] F. Alshmri, Rapid solidification processing: melt spinning of Al-High Si alloys, Adv. Mater. Res. 383–390 (2012) 1740–1746, https://doi.org/10.4028/www.scientific.net/AMR.383-390.1740.

[26] S.N. Grigoriev, T.V. Tarasova, G.O. Gvozdeva, S. Nowotny, Structure formation of hypereutectic Al-Si-alloys produced by laser surface treatment, J. Mech. Eng. 60 (6) (2014) 389–394, https://doi.org/10.5545/sv-jme.2013.1211.

[27] S.N. Grigoriev, T.V. Tarasova, G.O. Gvozdeva, S. Nowotny, Solidification behaviour during laser microcladding of Al-Si alloys, Surf. Coat. Technol. 268 (2015) 303–309, https://doi.org/10.1016/j.surfcoat.2014.08.001.

[28] S.N. Grigoriev, T.V. Tarasova, G.O. Gvozdeva, Optimization of parameters of laser surfacing of alloys of the Al-Si system, Met. Sci. Heat Treat. 57 (9) (2016) 589–595, https://doi.org/10.1007/s11041-016-9927-5.

[29] N. Ciftci, N. Ellendt, G. Coulthard, E. Soares Barreto, L. Mädler, V. Uhlenwinkel, Novel cooling rate correlations in molten metal gas atomization, Metall. Mater. Trans. B 50B (2019) 666–677, https://doi.org/10.1007/s11663-019-01508-0.

[30] C. Igathinathane, S.R. Methuku, Shape identification and particle size distribution from basic shape parameters using ImageJ, Comput. Electron. Agric. 63 (2) (2008) 168–182, https://doi.org/10.1016/j.compag.2008.02.007.

[31] R. Kumari, N. Rana, Particle size and shape analysis using imagej with customized tools for segmentation of particles, Int. J. Eng. Res. Technol. 4 (11) (2015) 247–250, https://doi.org/10.17577/IJERTTV4IS110211.

[32] J. König, S. Nolte, A. Tünnermann, Plasma evolution during metal ablation with ultrashort laser pulses, Opt. Express 13 (26) (2005) 10597–10607, https://doi.org/10.1364/OPEX.13.010597.

[33] Jerry L. Hudgins, Wide and narrow bandgap semiconductors for power electronics: a new valuation, J. Electron. Mater. 32 (6) (2003) 471–477, https://doi.org/10.1007/s11664-003-0128-9.

[34] W. Diagrams, H.Y. Fan, Infrared absorption in n-type silicon, Phys. Rev. 108 (2) (1957) 268–271. 10.1103/PhysRev.108.268.

[35] Martin A. Green, Mark J. Keevers, Optical properties of intrinsic silicon at 300 K, Prog. Photovolt. Res. Appl. 3 (1995) 189–192, https://doi.org/10.1002/pip.4670030303.

[36] S. Sundaram, E. Mazur, Inducing and probing non-thermal transitions in semiconductors using femtosecond laser pulses, Nat. Mater. 1 (2002) (2002) 217–224, https://doi.org/10.1038/nmat767.

[37] A. Rousse, C. Rischel, S. Fourmaux, I. Uschmann, S. Sebban, G. Grillon, P. Balcou, E. Foerster, J.P. Geindre, P. Audebert, J.C. Gauthier, D. Hulin, Non-thermal melting in semiconductors measured at femtosecond resolution, Nature 410 (2001) 65–68, https://doi.org/10.1038/35065045.

[38] R. Le Harzic, D. Breitling, M. Weikert, S. Sommer, C. Föhl, S. Valette, C. Donnet, E. Audouard, F. Dausinger, Pulse width and energy influence on laser micromachining of metals in a range of 100fs to 5ps, Appl. Surf. Sci. 249 (2005) 322–331, https://doi.org/10.1016/j.apsusc.2004.12.027.

[39] J.-C.M. Diels, W. Rudolph, Ultrashort Laser Pulse Phenomena: Fundamentals, Techniques, and Applications on a Femtosecond Time Scale, Elsevier, 2006, https://doi.org/10.1016/B978-0-12-215493-5.X5000-9.

[40] N. Saffari, A. Som, D.T. Green, Image processing techniques for improved porosity estimation, in: D.O. Thompson, D.E. Chimenti (Eds.), Review of Progress in Quantitative Nondestructive Evaluation, Springer, Boston, MA, 1993, https://doi.org/10.1007/978-1-4615-2848-7_115.

[41] P.T. Mannion, J. Magee, E. Coyne, G.M. O'Connor, T.J. Glynn, The effect of damage accumulation behaviour on ablation thresholds and damage morphology in ultrafast laser micro-machining of common metals in air, Appl. Surf. Sci. 233 (1–4) (2004) 275–287, https://doi.org/10.1016/j.apsusc.2004.03.229.

[42] M. Hashida, A.F. Semerok, O. Gobert, G. Petite, Y. Izawa, J.F. Wagner, Ablation threshold dependence on pulse duration for copper, Appl. Surf. Sci. 197–198 (2002) 862–867, https://doi.org/10.1016/S0169-4332(02)00463-4.

[43] C.S. Lee, N. Koumvakalis, M. Bass, Spot-size dependence of laser-induced damage to diamond-turned Cu mirrors, Appl. Phys. Lett. 41 (1982) 625–627, https://doi.org/10.1063/1.93629.

[44] J. Schille, L. Schneider, P. Lickschat, U. Loeschner, R. Ebert, H. Exner, High-pulse repetition frequency ultrashort pulse laser processing of copper, J. Laser Appl. 27 (2015), S28007, https://doi.org/10.2351/1.4906482.

[45] E. Marin, Characteristic dimensions for heat transfer, Lat. Am. J. Phys. Educ. 4 (1) (2010) 56–60.

[46] L.C. Wei, L.E. Ehrlich, M.J. Powell-Palm, C. Montgomery, J. Beuth, J.A. Malen, Thermal conductivity of metal powders for powder bed additive manufacturing, Addit. Manuf. 21 (2018) 201–208, https://doi.org/10.1016/j.addma.2018.02.002.

[47] S. Zhang, B. Lane, J. Whiting, K. Chou, On thermal properties of metallic powder in laser powder bed fusion additive manufacturing, J. Manuf. Process. 47 (2019) 382–392, https://doi.org/10.1016/j.jmapro.2019.09.012.

[48] T. Qi, H. Zhu, H. Zhang, J. Yin, L. Ke, X. Zeng, Selective laser melting of Al7050 powder: melting mode transition and comparison of the characteristics between the keyhole and conduction mode, Mater. Des. 135 (2017) 257–266, https://doi.org/10.1016/j.matdes.2017.09.014.

[49] T.W. Eagar, N.S. Tsai, Temperature-fields produced by traveling distributed heat-sources, Weld. J. 62 (1983) 346–355.

[50] D.C. Weckman, H.W. Kerr, J.T. Liu, The effects of process variables on pulsed Nd. YAG laser spot welds: part II. AA 1100 aluminum and comparison to AISI 409 stainless steel, Metall. Mater. Trans. B 28 (1997) 687–700, https://doi:10.1007/s11663-997-0043-1.

[51] W.E. King, H.D. Barth, V.M. Castillo, G.F. Gallegos, J.W. Gibbs, D.E. Hahn, C. Kamath, A.M. Rubenchike, Observation of keyhole-mode laser melting in laser powder-bed fusion additive manufacturing, J. Mater. Process. Technol. 214 (2014) 2915–2925, https://doi.org/10.1016/j.jmatprotec.2014.06.005.

[52] Y. Zhang, J.R.G. Evans, S. Zhang, Corrected values for boiling points and enthalpies of vaporization of elements in handbooks, J. Chem. Eng. Data 56 (2) (2011) 328–337, https://doi:10.1021/je1011086.

[53] W.E. King, H.G. Barth, V.M. Castillo, J.W. Gibbs, D. Hahn, C. Kamath, Observation of keyhole-mode laser melting in laser powder-bed fusion additive manufacturing, J. Mater. Process. Technol. 214 (12) (2013) 2915–2925, https://doi.org/10.1016/j.jmatprotec.2014.06.005.

[54] C. Weingarten, D. Buchbinder, N. Pirch, W. Meiners, K. Wissenbach, R. Poprawe, Formation and reduction of hydrogen porosity during selective laser melting of AlSi10Mg, J. Mater. Process. Technol. 221 (2015) 112–120, https://doi.org/10.1016/j.jmatprotec.2015.02.013.

[55] C. Zhao, N.D. Parab, X. Li, K. Fezzaa, W. Tan, A.D. Rollett, T. Sun, Critical instability at moving keyhole tip generates porosity in laser melting, Science 370 (6520) (2020) 1080–1086, https://doi:10.1126/science.abd1587.

[56] T.Y. Kuo, S.L. Jeng, Porosity reduction in Nd-YAG laser welding of stainless steel and inconel alloy by using a pulsed wave, J. Phys. D Appl. Phys. 38 (2005) 722–728, https://doi.org/10.1088/0022-3727/38/5/009.

[57] V. Vijeesh, K.N. Prabhu, Review of microstructure evolution in hypereutectic Al–Si alloys and its effect on wear properties, Trans. Indian Inst. Met. 67 (1) (2014) 1–18, https://doi.org/10.1007/s12666-013-0327-x.

[58] A. Leatham, A. Ogilvy, P. Chesney, J.V. Wood, Osprey process - production. Flexibility in materials manufacture, Met. Mater. 5 (3) (1989) 140–143. http://pascal-francis.inist.fr/vibad/index.php?action=getRecordDetail&idt=6728402.

[59] D. Apelian, H. Henein, U. Fritsching, Metal Sprays and Spray Deposition, Springer, Cham, 2017, https://doi.org/10.1007/978-3-319-52689-8_1.

[60] B.H. Kear. Cutting Edge Technologies, chapter Rapid Solidification Technology, The National Academy Press, Washington, D.C., 1984.

[61] Yali Li, Dongdong Gu, Parametric analysis of thermal behavior during selective laser melting additive manufacturing of aluminum alloy powder, Mater. Des. 63 (2014) 856–867, https://doi.org/10.1016/j.matdes.2014.07.006.

[62] T. DebRoy, H.L. Wei, J.S. Zuback, T. Mukherjee, J.W. Elmer, J.O. Milewski, A. M. Beese, A. Wilson-Heid, A. De, W. Zhang, Additive manufacturing of metallic components - process, structure and properties, Prog. Mater. Sci. 92 (2018) 112–224, https://doi.org/10.1016/j.pmatsci.2017.10.001.

[63] L.M. Hogan, H. Song, Interparticle spacings and undercoolings in Al-Si eutectic microstructures, Metall. Mater. Trans. A 18 (1987) 707–713, https://doi.org/10.1007/BF02649487.

[64] G.-h Meng, X. Lin Xin, W.-d Huang, Interlamellar spacing and average interface undercooling of irregular eutectic in steady-state growth, Trans. Nonferrous Met. Soc. China 18 (2) (2008) 405–409, https://doi.org/10.1016/S1003-6326(08)60071-0.

[65] Arnold Mauduit, Sébastien Pillot, Hervé Gransac, Study of the Suitability of Aluminum Alloys for Additive Manufacturing by Laser Powder-Bed Fusion, UPB Scientific Bulletin, Series B 79(4), 2017, 219–238. ISSN 1454–2331.

[66] P. Li, V.I. Nikitin, E.G. Kandalova, K.V. Nikitin, Effect of melt overheating, cooling and solidification rates on Al–16wt%Si alloy structure, Mater. Sci. Eng. A 332 (1) (2002) 371–374, https://doi.org/10.1016/S0921-5093(01)01864-0.

[67] H. Carslaw, J. Jaeger, Conduction of Heat in Solids, Oxford Science Publication, Oxford, UK, 1990.

[68] F.C. Robles Hernandez, J.M. Herrera Ramírez, R. Mackay, Al-Si Alloys - Automotive, Aeronautical, and Aerospace Applications, Springer International Publishing, 2017, https://doi.org/10.1007/978-3-319-58380-8.

[69] J. Zhou, H.-L. Tsai, Porosity formation and prevention in pulsed laser welding, J. Heat. Transf. 129 (8) (2007) 1014–1024, https://doi:10.1115/1.2724846.

[70] C.A. Biffi, J. Fiocchi, P. Bassani, A. Tuissi, Continuous wave vs pulsed wave laser emission in selective laser melting of AlSi10Mg parts with industrial optimized process parameters: microstructure and mechanical behavior, Addit. Manuf. 24 (2018) 639–646, https://doi.org/10.1016/j.addma.2018.10.021.